**Accepted Article Preview: Published ahead of online publication**

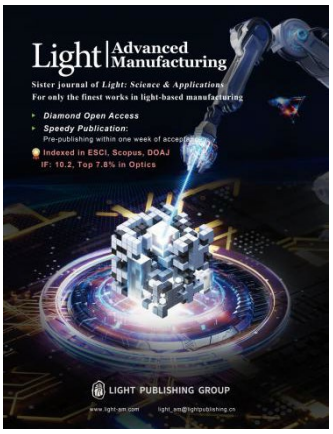


# Single-Layer Double-Sided Ultrawideband Near-Perfect Absorber Based on Biomimetic Metamaterial with Manufacturing Scalability, Flexible Transferability, and Environmental Stability

Sha Ouyang, Yanling Qiu, Chenchen Dong, Haixia Xu, Min Qiu, Meiyan Pan, Yihang Chen

Cite this article as: Sha Ouyang, Yanling Qiu, Chenchen Dong, Haixia Xu, Min Qiu, Meiyan Pan, Yihang Chen. Single-Layer Double-Sided Ultrawideband Near-Perfect Absorber Based on Biomimetic Metamaterial with Manufacturing Scalability, Flexible Transferability, and Environmental Stability. *Light: Advanced Manufacturing* accepted article preview 3 July, 2026; doi: 10.37188/lam.2026.120



Received 2 April 2026; revised 2 July 2026; accepted 3 July 2026;
Accepted article preview online 3 July 2026

# Single-Layer Double-Sided Ultrawideband Near-Perfect Absorber Based on Biomimetic Metamaterial with Manufacturing Scalability, Flexible Transferability, and Environmental Stability

**Sha Ouyang**[1,2,3], **Yanling Qiu**[1,2], **Chenchen Dong**[1,2], **Haixia Xu**[4], **Min Qiu**[5,6,7], **Meiyan Pan**[3, *], **Yihang Chen**[1,2, *]

[1] Key Laboratory of Atomic and Subatomic Structure and Quantum Control (Ministry of Education), School of Physics, South China Normal University, Guangzhou 510006, China

[2] Guangdong Provincial Key Laboratory of Quantum Engineering and Quantum Materials, Guangdong-Hong Kong Joint Laboratory of Quantum Matter, Frontier Research Institute for Physics, South China Normal University, Guangzhou 510006, China

[3] Ji Hua Laboratory, Foshan 528200, China

[4] College of Artificial Intelligence, Zhongkai University of Agriculture and Technology, Guangzhou 510225, China

[5] Zhejiang Key Laboratory of 3D Micro/Nano Fabrication and Characterization, School of Engineering, Westlake University, 18 Shilongshan Road, Hangzhou 310030, China

[6] Westlake Institute for Optoelectronics, Fuyang, Hangzhou 311421, China

[7] Institute of Advanced Technology, Westlake Institute for Advanced Study, Hangzhou 310024, China

*panmy@jihualab.ac.cn

*yhchen@scnu.edu.cn

## Abstract

Efficient light harvesting from front and rear sides is essential for improving solar energy utilisation in applications such as photovoltaics and seawater desalination. This requires absorbers that exhibit strong double-sided absorption in the ultraviolet to near-infrared range, mechanical flexibility for transfer onto diverse substrates, reliable performance stability, and manufacturing scalability for practical deployment. However, these capabilities are difficult to achieve simultaneously using conventional thin-film or metamaterial absorbers. In this study, we developed a double-sided bioinspired metamaterial absorber (DS-BMA) composed of a single layer of chromium (Cr) nano-units, whose front and back surfaces mimic the morphologies of moth eyes and marine diatoms, respectively. The gradient geometric configuration of the DS-BMA significantly broadened the bandwidths of plasmonic resonances, thereby enabling near-perfect absorption over the entire solar spectrum. Using a scalable self-assembly-based process, we experimentally showed a flexible, transferable DS-BMA with a thickness of 500 nm. It achieved average absorptances of 93% and 96% on the front and back sides, respectively, over a wavelength range of 220–2500 nm. The DS-BMA exhibited polarisation-independent omnidirectional absorption as well as excellent thermal stability, corrosion resistance, and mechanical robustness. Therefore, the DS-BMA is a promising route toward realizing high-efficiency, low-cost, and integrable double-sided solar absorbers and photothermal/photovoltaic energy conversion devices.

**Keywords:** Double-sided absorber, Biomimetic metamaterial, Ultrabroadband absorption, Scalable fabrication, Flexible transferable device

## Introduction

Achieving near-perfect absorption in the ultraviolet to near-infrared region is of great scientific and technological significance because such absorbers can effectively suppress both reflection and transmission. Accordingly, they provide an essential physical foundation for ultrahigh-precision spectral manipulation[1–3], efficient photothermal conversion[4–8], emerging stealth technologies[9–12], high-sensitivity sensing[13–16], and high-performance optoelectronic devices[17,18]. Continuous broadband absorption is particularly important for enhancing energy conversion efficiency in photothermal and optoelectronic applications.

With the advancements in nanotechnology, various structural strategies have been proposed to broaden the bandwidth of single-sided absorption[19]. For instance, carbon nanotube–metal nanowire composite arrays[20–23] achieve near-perfect absorption over an ultrabroad spectral range of 0.5–20 μm owing to their extremely high surface area and porous morphology. These properties enhance absorption through multiple scattering and nanoscale confinement effects. However, the overall thickness of these structures is typically much greater than the operating wavelength, which limits their integration into compact optical devices. As alternatives, metamaterial-based approaches have been developed by arranging and stacking resonant elements with different dimensions, either laterally or vertically[24–26], thereby extending the absorption bandwidth by the superposition of multiple resonance modes. However, such designs typically rely on advanced nanofabrication techniques, such as electron-beam lithography and focused ion beam milling, thereby resulting in a high fabrication cost, increased process complexity, and poor scalability.

Biomimetic structures include moth-eyes-like convex configurations[27–32] (which form effective refractive-index gradients to suppress interfacial reflection) and marine diatoms-inspired porous architectures[33–36] (which enhance broadband light harvesting through multiple scattering and photon localisation). Such structures have been

extensively explored to improve optical absorption. For example, Ren *et al.*[37] designed a metal–insulator–metal metamaterial featuring dual-coupled gradient resonant cavities inspired by cephalopod skin and insect compound eyes. This material achieved an average absorption of 93% over an ultrabroad spectral range of 200 nm–5 μm. Liao *et al.*[38] developed a honeycomb-like porous architecture based on a freestanding reduced graphene oxide and gold nanoparticle film inspired by the optical structure of crab compound eyes. This architecture exhibited broadband absorption as high as 95% in the 250–1000 nm range. Despite these advances, most reported broadband absorbers lack flexibility and transferability, and their designs are typically optimised only for front-side illumination, thereby causing the back side to exhibit a significantly reduced absorption efficiency.

By contrast, double-sided high-absorption architectures have greater potential for energy-related applications, such as seawater desalination and photovoltaic energy conversion[39–41]. For instance, Song *et al.*[42] developed a double-sided light-absorbing evaporator based on carbon/ceramic nanofilms and bilayer graphene, which enabled synergistic absorption of direct solar irradiation and water surface-reflected light, thereby significantly enhancing the evaporation rate and all-weather adaptability. Specifically, the double-sided evaporator achieved an evaporation efficiency of 156.06% under 1 sun illumination, corresponding to a four-fold increase in the evaporation rate compared with its single-sided counterpart. Yang *et al.*[43] fabricated high-efficiency double-sided Cu(In,Ga)$Se_2$ thin-film solar cells via a silver-assisted low-temperature process, which allowed effective light absorption and power generation from the front and rear surfaces. This approach significantly improves the overall energy yield and space utilisation efficiency of photovoltaic systems, thereby offering new opportunities for flexible, tandem, and building-integrated photovoltaic applications. Therefore, development of structures capable of achieving efficient broadband absorption in both incident directions is highly important. Although double-sided broadband absorption based on metamaterials has been shown in the terahertz regime[44], extension of these

concepts to shorter wavelengths, including the visible and near-infrared regions, remains challenging. This is because of the reliance on sophisticated lithographic processes and associated high fabrication costs. Until now, high-performance absorbers that simultaneously realise broadband, double-sided, near-perfect absorption from the ultraviolet to near-infrared spectrum while also offering flexibility and transferability have been rarely reported.

In this study, we developed an innovative single-layer double-sided bioinspired metamaterial absorber (DS-BMA). By integrating a moth-eye-inspired hexagonal nanopillar array with a marine diatom-inspired porous architecture into a single metallic layer, the developed structure achieved ultrabroadband and highly efficient absorption in the ultraviolet to near-infrared range (220–2500 nm). Benefiting from the complementary gradient geometries of the top and bottom surfaces, the absorption bandwidth was significantly broadened while maintaining a simple structural configuration. The DS-BMA was flexible and transferable by polyethylene terephthalate (PET) encapsulation. The experimental results showed that the encapsulated absorber achieved average absorption efficiencies as high as 93% and 96% for front- and back-side illumination, respectively, within the target spectral range (94% and 96% in the AM1.5 solar spectrum), indicating excellent broadband absorption performance. Infrared thermography measurements were performed under one-sun illumination to further evaluate the photothermal conversion capability. After radiometric correction based on experimentally determined emissivity, the steady-state temperatures were determined to be 76.2 °C and 73.3 °C for the front and back sides, respectively. In addition, the structure exhibited polarisation-insensitive and wide-angle absorption characteristics. Experimental measurements showed that the average absorption remained above 90% for transverse-electric and transverse-magnetic polarisations in the entire ultraviolet to near-infrared range with negligible polarisation-dependent variation. Furthermore, high absorption efficiencies exceeding 85% were maintained for incident angles up to 60° for both front- and back-side illumination. The

absorber also exhibited excellent operational stability with no observable degradation in the optical performance after repeated bending, long-term ambient exposure, and thermal cycling tests. After 24 h of immersion in dilute sulfuric acid, the encapsulated device maintained its structural integrity, with the absorption degradation limited to 0.47% and 1.74% at the front and back sides, respectively. Following accelerated aging at 150 °C for 5 h, the band-averaged variations were limited to approximately 0.09% and 2.59% for front-side and back-side illumination, respectively. After 500 bending cycles, the band-averaged absorptance changed by less than 0.13% and 0.25% for front- and back-side illumination, respectively. From a fabrication perspective, self-assembly has proven to be a cost-effective mass-production method and has been widely applied to single-sided absorbers[45]. In this study, we extended the application of this technique to double-sided absorbers. The combination of colloidal self-assembly and magnetron sputtering enabled large-area scalable production and flexible transfer was realized via substrate peeling, thereby significantly enhancing the adaptability of the device for diverse application scenarios.

## Results and Discussion

### Structural Design

As shown in Figure 1a,b, the design concept is inspired by biomimetic principles in which a moth-eye-inspired hexagonal nanopillar array with gradient features is combined with a marine-diatom-inspired porous structure. This results in a composite gradient biomimetic architecture featuring a hemispherical protrusion array on the top surface and a hemispherical cavity array on the bottom surface, as shown in Figure 1c. The unit cell of the DS-BMA is periodically arranged in a hexagonal lattice with side length $L$ and overall thickness $H$. The hemispherical protrusions and cavities on the top and bottom surfaces share the same diameter $D$ and are periodically distributed with a

lattice period *P*.

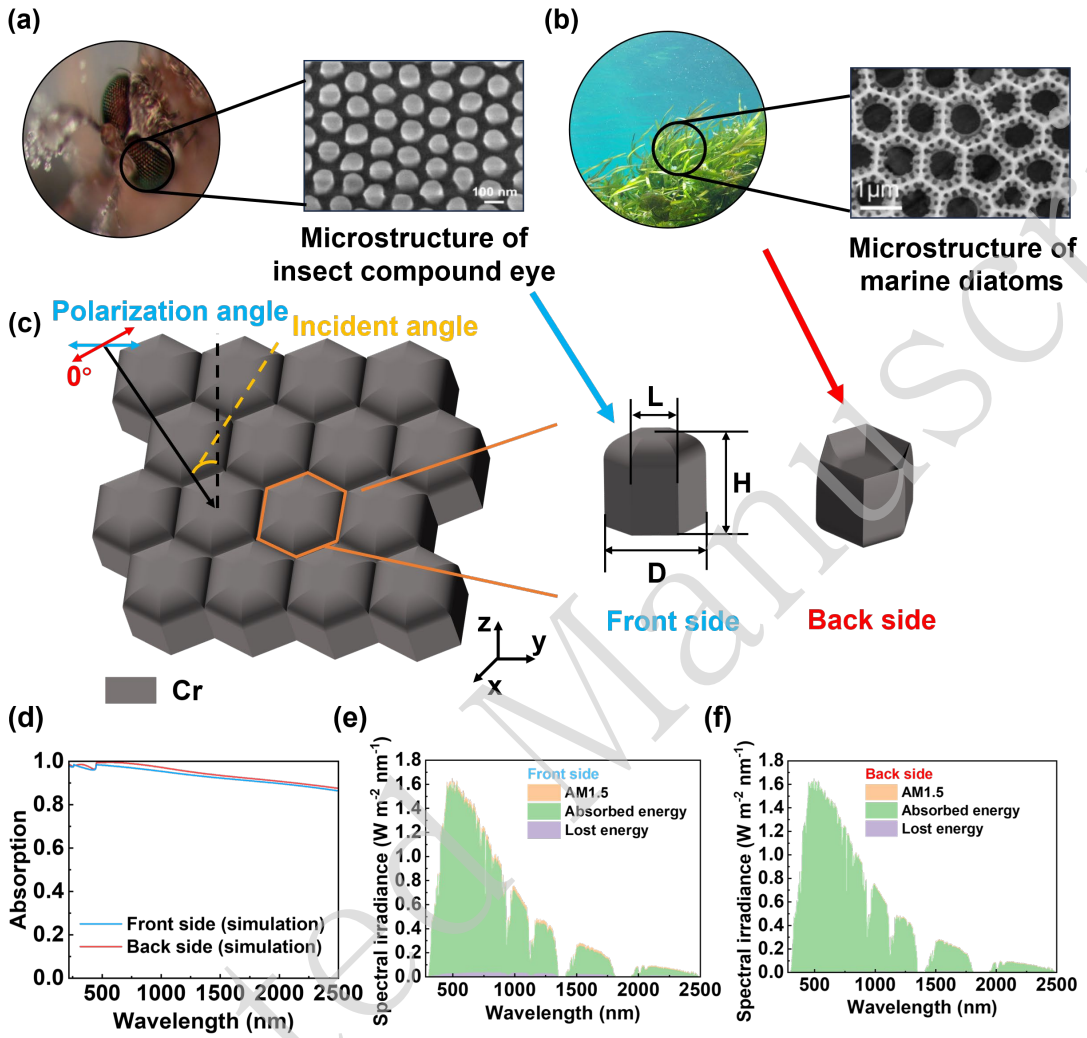


**Figure 1. Structure design and absorption performance. a**, Microstructure of the moth-eye compound eye.[46] Copyright 2007, Wiley. **b**, Microstructure of marine diatoms.[36] Copyright 2007, Wiley. **c**, Schematic of the biomimetic metamaterial absorber structure. **d**, Simulated absorption spectrum of the metamaterial absorber. **e**, Simulated absorption and energy loss spectra on the front and **f**, back sides in the AM1.5 solar spectrum.

Chromium (Cr) was chosen as the constituent material because of its large imaginary part in the dielectric function in the ultraviolet to near-infrared region, where terrestrial solar radiation is primarily concentrated. Moreover, compared with noble metals such

as gold and silver, chromium offers advantages such as lower cost and more mature fabrication processes, thereby making it more suitable for large-scale applications.

After systematic optimisation (Figure S1, Supporting Information), the optimal structural parameters were determined as $P$ = 520 nm, $D$ = 500 nm, $L$ = 290 nm, and $H$ = 500 nm. Consequently, as shown in Figure 1d, the simulated average absorption efficiencies of the freestanding Cr nanostructure reach 93% and 94% for front and back-side illumination, respectively. In the AM1.5 solar spectrum, the corresponding average absorption efficiencies further increase to 96% and 98%, respectively, as shown in Figure 1e,f (the calculation method for the AM1.5 spectrum is provided in Supporting Information S2).

**Absorption Mechanism**

To gain deeper insight into the physical origin of the ultrabroadband absorption, electromagnetic simulations were performed to analyse the field distributions of the developed DS-BMA at three representative wavelengths of 500, 1500, and 2500 nm. As shown in Figure 2, the ultrabroadband absorption arises primarily from the synergistic interplay between surface plasmon resonances and magnetic polariton excitations. In addition, the unique gradient geometry, which is characterised by a continuous transition from hemispherical protrusions on the top surface to hemispherical cavities on the bottom surface, facilitates excitation of multiple resonant modes at different wavelengths. Therefore, the absorption bandwidth is effectively extended from the ultraviolet to the near-infrared region. To quantitatively distinguish the contribution of the surface structure from the intrinsic material loss, the optical constants ($n$ and $k$) of the sputtered Cr film and absorption spectrum of a 1000-nm-thick planar Cr film were systematically characterised (Figure S2, Supporting Information). The planar Cr film exhibited an average absorptance of only 68.1% over the wavelength range of 220–2500 nm. Although the large extinction coefficient ($k$) of

Cr ensured strong optical dissipation and negligible transmission, it also caused considerable reflection owing to the impedance mismatch at the air/Cr interface. By contrast, the biomimetic micro/nanostructure reduced the reflection loss by a smoother optical transition and promotes multiple light–matter interactions within the structure. Consequently, the average absorptance exceeded 93%. Therefore, the observed near-perfect absorption originates from the synergistic contribution of the intrinsic loss of Cr and structural modulation of the optical field.

At the shorter wavelength of λ = 500 nm, pronounced electric and magnetic field localisation is observed near the top surface of the structure, as shown in Figure 2a and b. This indicates excitation of surface plasmon resonances at the chromium–air interface. Enhanced magnetic fields are also detected along the sidewalls of the absorber, which can be attributed to the excitation of magnetic polaritons. These two mechanisms work cooperatively to confine the electromagnetic energy to the upper surface and sidewall regions of the Cr layer. Owing to the intrinsically high optical loss of Cr, the localised electromagnetic energy is efficiently dissipated within the metal, which results in strong absorption in the short-wavelength regime. At the intermediate wavelength of λ = 1500 nm, the magnetic field enhancement is predominantly concentrated along the sidewall regions (Figure 2b), which indicates that magnetic polaritons become the dominant absorption mechanism in this spectral range. This magnetic resonance behaviour can be described well using an equivalent LC circuit model (Figure S3, Supporting Information). In this model, the Cr nanostructure acts as an effective nanoinductor ($L$), whereas the air gaps between adjacent Cr units and the air-filled recessed regions within the structure serve as effective nanocapacitors ($C$). Under this framework, the resonance wavelength of the magnetic polaritons can be approximately expressed as $\lambda \approx 2\pi c_0\sqrt{LC}$. Importantly, the complementary gradient geometry leads to wavelength-dependent variations in the effective inductive and capacitive responses along the vertical direction. Consequently, magnetic polariton

resonances can be excited at different spatial locations for different spectral ranges, which collectively contribute to the observed ultrabroadband absorption in a single metallic layer. For front-side illumination, the effective capacitance *C* increases as the interparticle gaps and metal separations decrease along the vertical direction, which leads to a redshift in the magnetic polariton resonance. Consequently, with increasing incident wavelength, the localisation region of the magnetic polaritons gradually shifts downward along the sidewalls. When an electromagnetic wave is incident from the back side, the underlying physical mechanisms remain essentially the same, with surface plasmon resonances and magnetic polaritons still playing dominant roles. The primary difference lies in the composition of the effective capacitance *C*, which is mainly determined by the air regions enclosed by the hemispherical chromium cavities on the lower surface. This complementary capacitive configuration enables efficient excitation of the resonant modes under reverse illumination, thereby ensuring high absorption from both sides.

Notably, as shown in the comparative simulations in Figure 2e,f, introducing nanoscale gaps between adjacent polystyrene (PS) spheres significantly enhances the absorption compared with the ideal close-packed structure without gaps. This improvement can be attributed to several factors. First, the nanoscale gaps create a strong capacitive coupling between neighbouring metallic units, which significantly enhances the local electric fields. Second, these gaps electrically isolate adjacent units, thereby enabling the formation of pronounced loop currents that strengthen the magnetic polariton resonances, which are particularly critical for near-infrared absorption. Finally, the presence of nanoscale gaps optimises the overall effective impedance of the structure and improves the impedance matching with free space over a broader spectral range, thereby suppressing reflection more effectively. To further clarify the representative dimensions, a nominal nanogap of 20 nm observed in our experimental samples is adopted for the electric field distributions shown in Figure 2e,f. Regarding large-area manufacturing controllability, these nanoscale gaps are naturally

formed owing to the physical self-limiting nature of sphere packing and subsequent shadowing effect during magnetron sputtering.[47] Statistical analysis based on different fabrication batches (Supporting Information Figure S4) showed a relatively concentrated nanogap distribution centred at ~20 nm, which supports the reasonable uniformity of the experimentally observed gap feature. Although this bottom-up approach exhibits minor fluctuations compared with high-precision lithography, the optical performance of the developed metasurface remains highly tolerant to such variations. The parametric simulation results in Figure 2g,h show that the 20 nm gap delivers the optimal absorption performance, whereas structures with gap sizes ranging from 10 to 30 nm still maintain band-averaged absorptances exceeding 90.8%/91.5% (front/back) in the 220–2500 nm range. Therefore, these structures with a gap substantially outperform the gapless reference structure (87.9%/86.5%). This broad tolerance window indicates that moderate fabrication-induced gap variations do not severely degrade the broadband light-harvesting capability, thereby reinforcing the robustness and scalability of the developed fabrication strategy.

Because of the highly symmetric geometric design, the absorption spectra remained essentially identical under different polarisation states (Figure S5, Supporting Information). Moreover, the absorber maintained an average absorption exceeding 80% over a wide incident angle range of 0–60° (Figure S5, Supporting Information), which exhibits its excellent angular insensitivity. These characteristics render the developed structure particularly suitable for practical light-harvesting applications involving unpolarized and obliquely incident solar radiation.

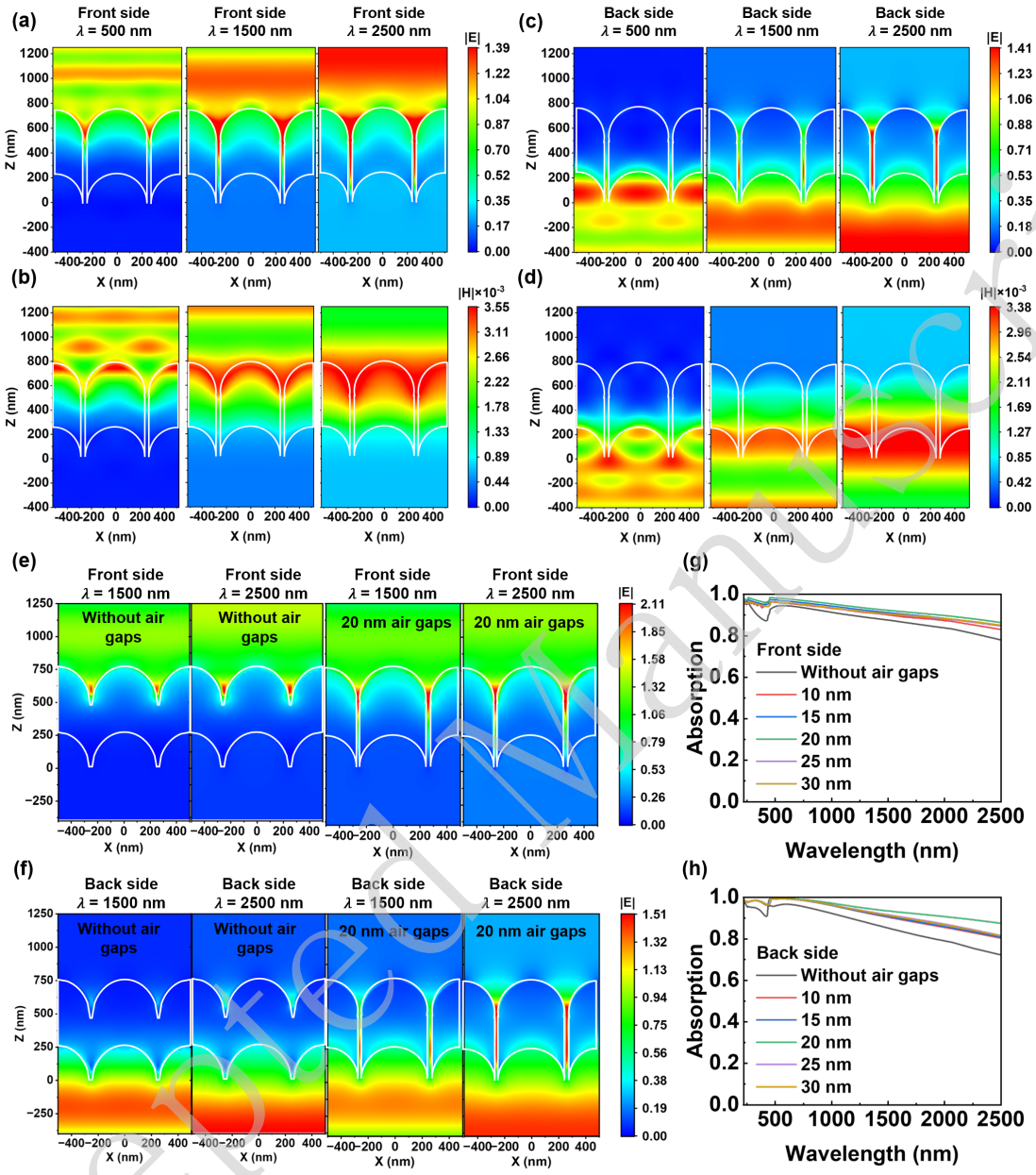


**Figure 2. Electromagnetic response mechanism of the broadband absorption. a**, Electric field and **b,** magnetic field distributions on the front side of the biomimetic metamaterial absorber at 500 nm, 1500 nm, and 2500 nm wavelengths. **c,** Electric field and **d,** magnetic field distributions on the back side at the same wavelengths. **e,** Comparison of the electric field distributions on the front and **f,** back sides of the single-layer Cr structures with a representative nanogap of 20 nm at wavelengths of 1500 nm and 2500 nm. **g,** Absorption spectra on the front and **h,** back sides of the single-layer Cr structures with various nanogap sizes (gap = 10, 15, 20, 25, and 30 nm) and reference structure without air gap.

**Sample Fabrication and Characterization**

A lithography-free fabrication strategy was developed for the preparation of the metamaterial absorber (Figure 3a; Figure S6 and S7 in Supporting Information), which could be flexibly transferred using a transparent PET adhesive tape. As shown in Figure 3a, first, a highly ordered monolayer array of PS microspheres with a diameter of 500 nm is assembled on a silicon substrate by combining gas–liquid interfacial self-assembly with the Langmuir–Blodgett technique. This method forms a regular two-dimensional photonic crystal template. Subsequently, a 500 nm-thick Cr film is deposited onto the PS template via magnetron sputtering, thereby resulting in a PS–Cr composite structure. After thermal treatment at 400 °C for 2 h to remove the PS template, the metamaterial absorber is non-destructively transferred using a PET adhesive tape. The PET adhesive tape exhibits excellent flexibility, thereby endowing the transferred absorber with outstanding bending tolerance. Its high optical transparency and reliable adhesion preserve the intrinsic optical properties of the metamaterial in the visible to near infrared wavelength range (Text S8 in the Supporting Information) while ensuring stable attachment to various target substrates. This fabrication approach, which integrates template-assisted patterning with flexible transfer technology, offers a versatile route for applying metamaterial absorbers to curved optical components and wearable devices. In this study, this approach was implemented on samples with dimensions of up to 2 cm × 2 cm, which was the maximum size achievable using the current laboratory setup. However, similar gas–liquid interfacial self-assembly methods have been extended to wafer-scale fabrication, which indicates the scalability potential of the underlying assembly strategy[45].

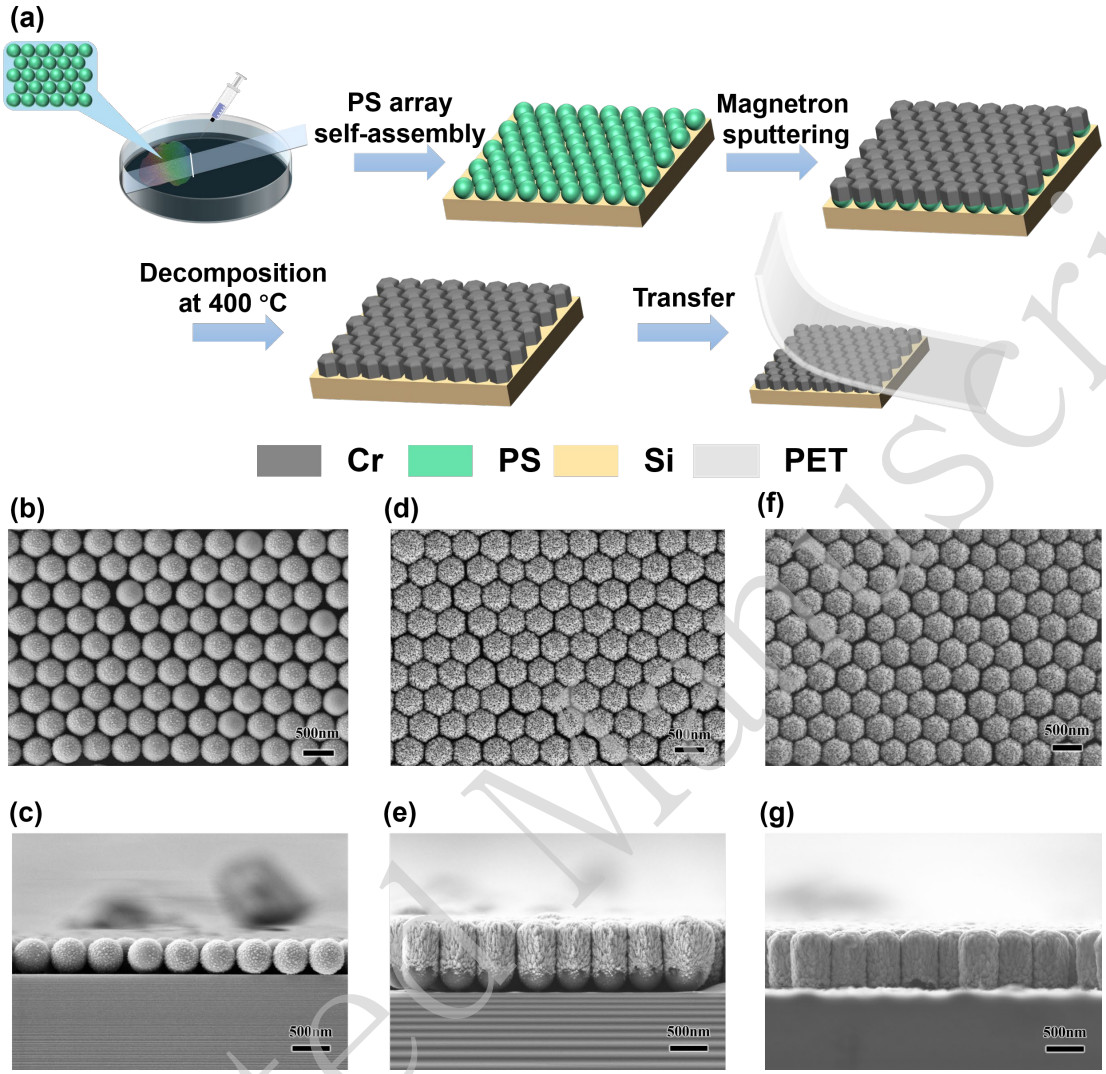


**Figure 3. Fabrication process and structural characterization. a,** Schematic of the fabrication process of the biomimetic metamaterial absorber. SEM images of a **b-c,** single-layer periodic PS microsphere array, **d-e,** PS array after Cr deposition, and **f-g,** DS-BMA sample.

The surface morphologies of the samples were characterised using scanning electron microscopy (SEM), and SEM images are shown in Figure 3b,g and Figure S8 (Supporting Information). Because of the intrinsic characteristics of magnetron sputtering and monolayer PS microsphere template, nanoscale gaps of approximately 20 nm are formed between adjacent microspheres. Although such gaps are generally regarded as unavoidable microstructural imperfections in experiments, the preceding mechanism analysis indicates that these nanoscale gaps enhance light scattering and

electromagnetic confinement, thereby improving the overall optical absorption performance. In addition, owing to the relatively large size of the Cr clusters generated during direct-current sputtering, the deposited Cr layer exhibits a discontinuous morphology. Compared with continuous metallic films, discontinuous chromium structures generally possess higher optical absorption and reduced intrinsic film stress, which significantly improves the success rate of the subsequent transfer process. Collectively, these structural features lead to the efficient light harvesting and robust flexible transfer of the metamaterial absorber.

**Absorption Performance Analysis**

The absorption of the fabricated DS-BMA was measured using an ultraviolet–visible–near-infrared spectrophotometer. As shown in Figure 4a, the absorber exhibits outstanding broadband near-perfect absorption in the 220–2500 nm, with measured average absorption efficiencies of 93.8% and 96.1% for front- and back-side illumination, respectively. These experimental results are in excellent agreement with the simulated predictions, thereby validating the effectiveness of the developed design. As shown in Figure 4b–d, systematic characterisation further exhibits that the absorber maintains high absorption under different polarisation states. Moreover, stable absorption performance occurs over a wide incident angle range of 0–60°, thereby confirming the excellent polarisation-insensitive and wide-angle absorption characteristics of the device. In addition, the absorption performance in the standard AM1.5 solar spectrum was evaluated using the measured spectra. As shown in Figure 4e,f, the average absorption efficiencies reach 94% and 96% for front- and back-side illumination, respectively, which highlights the significant potential of the absorber for efficient solar energy harvesting and photothermal utilisation. Supporting Information Table S1 summarises the key performance metrics of representative broadband absorbers reported in recent literature. Compared with these broadband absorbers, our

device simultaneously exhibits a broader effective absorption bandwidth and higher average absorptance over the solar spectrum. Near-perfect absorption exceeding 93% is achieved on both the front and back sides throughout the ultraviolet–visible–near-infrared region. Compared to most previously reported structures, which realise high absorption only under single-sided illumination or within limited spectral ranges, the developed single-layer DS-BMA offers clear advantages in terms of the absorption bandwidth, dual-sided absorption symmetry, and structural simplicity. Moreover, the developed absorber does not rely on complex multilayer stacking or sophisticated lithographic processes and still exhibits excellent flexibility and transferability together with a strong potential for large-area fabrication. Therefore, it is superior to existing broadband absorbers in terms of overall performance and practical applicability.

To further evaluate the photothermal conversion capability of the DS-BMA, photothermal heating experiments were performed under standard one-sun illumination (AM1.5, 1000 W $m^{-2}$). A calibrated solar simulator was employed to ensure spatially uniform and temporally stable irradiation. The use of a standard one-sun condition eliminated regional and seasonal variations in the natural solar irradiance, thereby providing a reproducible and location-independent evaluation platform[48]. To minimise conductive heat loss and accurately capture the true thermal equilibrium, a flexible sample was suspended in ambient air using a minimal metal frame support and avoiding any direct contact with solid surfaces that could act as thermal sinks. The front and back sides of the sample were separately exposed to identical irradiation conditions. Starting from room temperature (25 °C), the sample heated rapidly and reached a steady-state equilibrium after approximately 15 min. A precise radiometric calibration based on the experimentally measured mid-infrared emissivity spectra was performed (detailed in Supporting Information S12). As shown in Figure 4g,h, the true equilibrium temperatures reach 76.2 °C and 73.3 °C under front- and back-side illumination, respectively. Notably, once equilibrium is reached, the temperatures remain nearly constant for more than 90 min under continuous one-sun irradiation, which shows

excellent photothermal stability. The comparable temperature rise under front- and back-side illumination further confirms the effective dual-sided solar absorption and efficient light-to-heat conversion capability of the DS-BMA, which highlights its strong potential for solar-driven photothermal applications (see Supporting Information S12 for a detailed analysis).

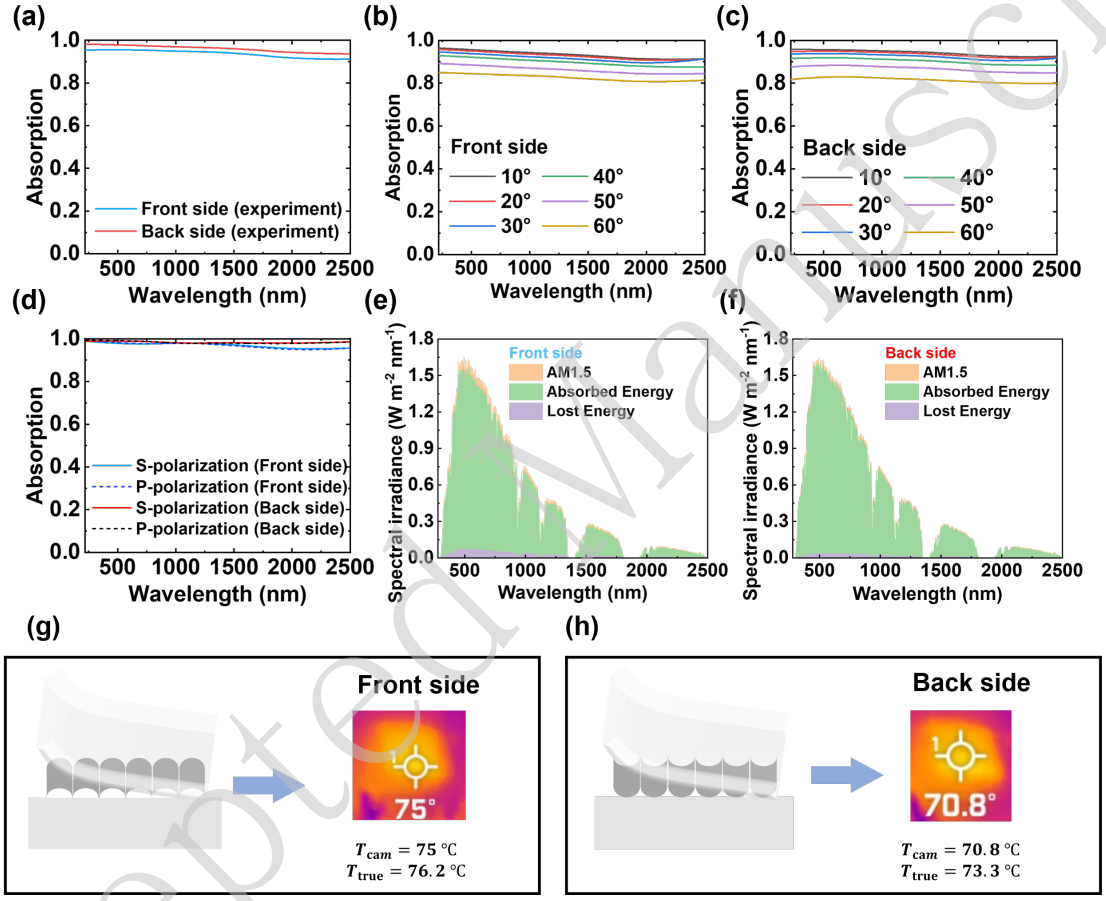


**Figure 4. Broadband absorption characterization. a,** Absorption spectra of the DS-BMA sample under normal incidence. **b,** Absorption spectra for the front and **c,** back sides of the DS-BMA at different incident angles. **d,** Absorption spectra under polarized light. **e,** Absorption spectra for the front and **f,** back sides in the AM1.5 solar spectrum. **g,** The temperature of the front and **h,** back sides of the DS-BMA absorber in thermal equilibrium under 1 sun.

## Stability Tests

To evaluate the reliability of the double-sided absorber under practical operating

conditions, comprehensive environmental and mechanical stability tests were conducted; the specific test data are listed in Table 1. Owing to the flexible PET-based encapsulation and transfer layer, the absorber can be conformally laminated onto nonplanar or flexible surfaces, including curved, folded, or slightly textured substrates, without inducing structural damage or performance degradation, as shown in Figure 5a. The PET provides sufficient mechanical support to accommodate bending and deformation while simultaneously serving as a protective barrier that shields the Cr nanostructures from direct chemical and physical damage. This combination enables robust integration of the absorber into complex application scenarios.

Corrosion resistance was evaluated by immersing the encapsulated device in a highly concentrated sulfuric acid solution (18 mol $L^{-1}$) for 24 h. As shown in Figure 5b, after exposure, the absorber maintains its structural integrity and optical performance. The band-averaged absorptance over the wavelength range of 220–2500 nm decreases only slightly from 93.78% to 93.31% for front-side illumination and from 96.06% to 94.33% for back-side illumination (Figure 5b), corresponding to absolute variations of 0.47% and 1.74%, respectively. These results show the excellent chemical stability and corrosion resistance of the encapsulated DS-BMA in harsh acidic environments.

Thermal stability was assessed by conducting accelerated aging tests at 150 °C for 5 h. This temperature was selected by considering the high melting point of Cr (~1800 °C) and thermal tolerance of the current encapsulation tape (~200 °C). As shown in Figure 5c, the broadband absorption performance remains stable after heating. The band-averaged absorptance over 220–2500 nm exhibits only a negligible decrease of 0.09% for front-side illumination, whereas the back-side absorptance shows a slight increase of 2.59%, indicating excellent thermal robustness of the absorber. Notably, the operational temperature limit of the device can be further extended by employing encapsulation materials with a higher thermal endurance.

The mechanical stability was further examined by conducting bending durability

tests over 500 bending cycles. As shown in Figure 5d, the band-averaged absorptance remains essentially unchanged after repeated mechanical deformation, with variations of only 0.13% for front-side illumination and 0.25% for back-side illumination. These negligible changes confirm the excellent mechanical robustness of the double-sided absorber and show that its ultrabroadband absorption performance is preserved well under repeated bending and deformation.

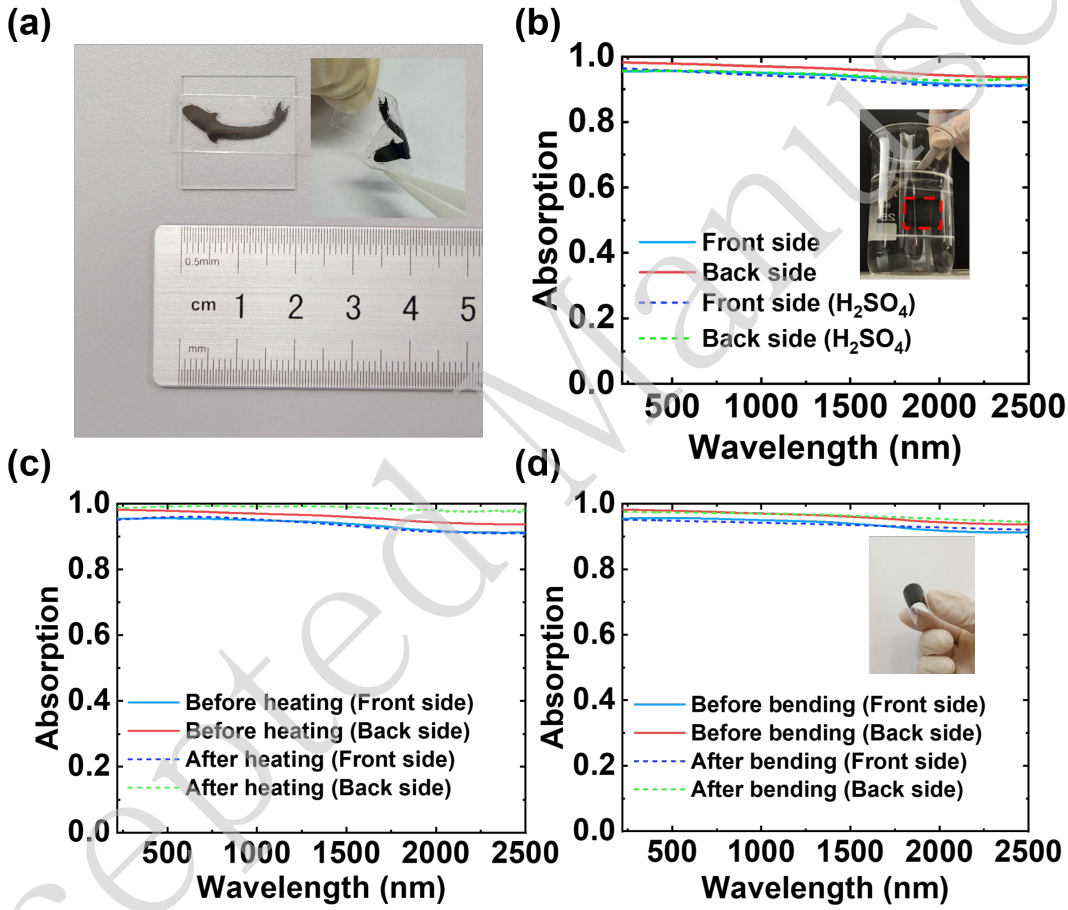


**Figure 5. Performance stability under different environments. a,** Images of the DS-BMA after patterning. Absorption spectra of the DS-BMA before and after **b,** corrosion resistance test, **c,** thermal stability test at 150 °C, and **d,** mechanical bending durability test for 500 cycles.

**Table 1.** Summary of the stability tests of the double-sided absorber

| Test methods | Measured Band-averaged Absorption over 220–2500 nm | | | |
|---|---|---|---|---|
| | **Illumination side** | **Before (%)** | **After (%)** | **Absolute change (%)** |
| Corrosion resistance (24 h immersion in sulfuric acid) | Front side | 93.78 | 93.31 | −0.47 |
| | Back side | 96.06 | 94.33 | −1.74 |
| Thermal stability (150 °C, 5 h) | Front side | 93.78 | 93.69 | −0.09 |
| | Back side | 96.06 | 98.65 | +2.59 |
| Bending durability (500 cycles) | Front side | 93.78 | 93.65 | −0.13 |
| | Back side | 96.06 | 96.32 | +0.25 |

## Conclusion

We developed a single-layer double-sided biomimetic metamaterial absorber tailored to the solar spectrum. Owing to the synergistic effects of surface plasmon resonances and magnetic polariton excitations, the absorber achieves excellent broadband absorption over the wavelength range of 220–2500 nm, with average absorption efficiencies of 93% and 96% for front-side and back-side illumination, respectively. Because of its simple structural configuration, compatibility with manufacturing fabrication, and flexible transferability, the developed absorber can be

readily adapted to diverse application scenarios. The device exhibits omnidirectional polarization-insensitive absorption, outstanding thermal stability, corrosion resistance, and mechanical robustness, thereby ensuring reliable operation under complex environmental conditions. Importantly, beyond Cr, other low-cost metals with high intrinsic optical losses, such as titanium, may also achieve comparable broadband absorption performance by appropriate structural optimisation, thereby providing additional flexibility for material selection in future studies. These features render the developed absorber highly attractive for applications requiring efficient double-sided light capture and a broadband spectral response, including bifacial photovoltaic devices, solar-driven interfacial desalination systems, and emerging multifunctional photothermal regulation platforms.

## Materials and Methods

### Materials

Monodisperse PS microspheres with a diameter of 500 nm were purchased from Shanghai Huizhi Biotechnology Co., Ltd. Sodium dodecyl sulphate (SDS) was obtained from Shanghai Beyotime Biotechnology Co., Ltd. High-purity Cr sputtering targets were supplied by Zhongnuo Advanced Material (Beijing) Technology Co., Ltd. The transparent adhesive tape used for the transfer consisted of polyacrylate adhesive and PET backing layers and was purchased from Foshan Xinfengshang New Materials Technology Co., Ltd. All the materials were used as received without further purification.

### Preparation of PS Microsphere Monolayer Mask

A PS microsphere monolayer mask was prepared via gas–liquid interfacial self-assembly. Briefly, 0.1 mL of aq. 5 wt% suspension of 500 nm PS microspheres was diluted with anhydrous ethanol at a volume ratio of 1:2 and ultrasonicated for 60 s to

obtain a uniformly dispersed suspension. A rectangular glass substrate was then placed obliquely (≈30°) in 400 mL of deionised water, followed by addition of 20 μL of 10 wt% SDS solution to reduce the surface tension of the aqueous phase. After stabilization of the water surface, the PS microsphere suspension was slowly injected along the inclined glass substrate into the water phase at a constant rate of 0.4 μL $s^{-1}$ using a microsyringe pump. Driven by the Marangoni effect at the air–water interface and surfactant action of SDS, the PS microspheres spontaneously assembled into a highly ordered hexagonally close-packed monolayer at the water surface. The assembled monolayer was subsequently transferred onto a 2 cm × 2 cm silicon substrate using the Langmuir–Blodgett technique and allowed to dry naturally.

**Cr Deposition and Mask Removal**

Cr was deposited using a high-vacuum magnetron sputtering system (ATTO 10). The PS microsphere monolayer samples were fixed on a sample holder and aligned parallel to a Cr target with a purity of 99.99%. After the base pressure of the chamber reached $5 \times 10^{-5}$ Pa, high-purity argon gas (99.999%) was introduced at a flow rate of 20 sccm to maintain a working pressure of $6.8 \times 10^{-2}$ Pa. Direct-current sputtering was performed at 50 W for 1 h at 25 °C, which yielded a Cr layer with a thickness of approximately 500 nm. The PS microsphere mask was subsequently removed by thermal treatment. Specifically, the samples were placed in a tube furnace (CAD) and heated to 400 °C at a ramping rate of 9 °C $min^{-1}$ under an argon flow of 500 sccm, followed by annealing for 2 h to ensure complete decomposition of the PS spheres. The samples were naturally cooled to room temperature, which yielded a pure Cr layer with periodic micro/nanostructures.

**Transfer and Encapsulation of the Metamaterial Absorber**

A transparent PET adhesive tape was employed as the transfer medium for efficient transfer and encapsulation of the metamaterial absorber. Specifically, the PET tape was gently laminated onto the fabricated absorber surface under moderate pressure to

ensure intimate contact, followed by slow peeling to completely transfer the absorber onto the tape. The transferred absorber was attached to the desired target substrate. This simple transfer process effectively preserved the structural integrity and optical performance of the absorber, thereby enabling its facile integration onto substrates with various shapes.

**Characterization**

The microstructural morphology of each fabricated metamaterial absorber was characterised using field-emission SEM (FESEM; ZEISS Ultra 55). The optical properties were measured using an ultraviolet–visible–near-infrared spectrophotometer (SolidSpec-3700, Shimadzu) over a wavelength range of 220–2500 nm, from which the reflectance and transmittance spectra were obtained. All the optical measurements were conducted at room temperature.

**Numerical Simulations**

Numerical simulations were performed using the finite-difference time-domain method to investigate the optical response of the metamaterial absorber. Because the PET transfer layer was not part of the original absorber design, it is not included in the simulations described in the main text. Additional simulations incorporating the PET layer are discussed in Supporting Information S8. The results showed that it mainly functions as a mechanically supportive and protective encapsulation layer and introduces only a minor optical contribution within the investigated spectral range. The optical constants (refractive index $n$ and extinction coefficient $k$) of Cr were obtained from experimentally measured ellipsometry data to ensure accurate material modelling. According to the law of energy conservation, absorption (A) was calculated as $A = 1 - R - T$, where R and T denote the reflectance and transmittance, respectively. Periodic boundary conditions were applied in the x- and y-directions to simulate an infinite periodic array, whereas perfectly matched layer boundary conditions were used along the z-direction to eliminate nonphysical reflections. The

spatial mesh resolution of the simulation region was set to 4 nm.

## Acknowledgements

This work was supported by the Natural Science Foundation of Guangdong Province (2024A1515012296 and 2025A1515011712) and the Guangzhou Municipal Science and Technology Project (2019050001). The authors gratefully acknowledge Dr. Huanzheng Zhu of Zhejiang University for his valuable assistance in mid-infrared spectral measurements.

## Author Contributions

S. Ouyang and Y. Qiu contributed equally to this study. S. Ouyang: Writing – original draft, Resources, Methodology, Investigation, Formal analysis, Conceptualization. Y. Qiu: Visualization, Validation, Software, Resources, Investigation. C. Dong: Visualization, Validation, Software, Resources, Investigation. H. Xu: Visualization, Project administration, Methodology. M. Qiu: Writing – review & editing. M. Pan: Writing – review & editing, Visualization, Supervision, Project administration, Methodology, Funding acquisition, Conceptualization. Y. Chen: Writing – review & editing, Visualization, Supervision, Project administration, Methodology, Funding acquisition, Conceptualization.

## Data Availability

The data supporting the findings of this study are available from the corresponding author upon request.

## Conflict of interest

The authors declare no competing interests.

## Supplementary information

Supplementary materials are available at the online version.

## References


1. Tian, J. Y. et al. High- *Q* all-dielectric metasurface: super and suppressed optical absorption. *ACS Photonics* **7**, 1436-1443 (2020).
2. Pan, M. Y. et al. Multi-band middle-infrared-compatible camouflage with thermal management via simple photonic structures. *Nano Energy* **69**, 104449 (2020).
3. Fu, B. et al. Wavelength tunable pulsed lasers enabled by a versatile metafiber functioning as both saturable absorber and filter. *Advanced Science* **13**, e11572 (2026).
4. Liu, J. et al. All-day uninterrupted thermoelectric generator by simultaneous harvesting of solar heating and radiative cooling. *Optics Express* **31**, 14495-14508 (2023).
5. Zhou, L. et al. 3D self-assembly of aluminium nanoparticles for plasmon-enhanced solar desalination. *Nature Photonics* **10**, 393-398 (2016).
6. Khodasevych, I. E. et al. Micro- and nanostructured surfaces for selective solar absorption. *Advanced Optical Materials* **3**, 852-881 (2015).
7. Li, F. F. et al. Polarization-dependent wideband metamaterial absorber for ultraviolet to near-infrared spectral range applications. *Optics Express* **30**, 25974-25984 (2022).
8. Ying, Y. B. et al. Photonic control of thermal radiation for protective windows. *Light*: *Advanced Manufacturing* **6**, 34 (2025).
9. Grady, N. K. et al. Terahertz metamaterials for linear polarization conversion and anomalous refraction. *Science* **340**, 1304-1307 (2013).
10. Zhu, R. X. et al. Digital camouflage encompassing optical hyperspectra and thermal infrared-terahertz-microwave tri-bands. *Nature Communications* **16**, 8112 (2025).
11. Zhao, M. et al. High-temperature stealth across multi-infrared and microwave bands with efficient radiative thermal management. *Nano-Micro Letters* **17**, 199 (2025).
12. Qin, R. et al. Multi-dimensional camouflage against VIS-NIR hyperspectral, MIR intensity, and MIR polarization imaging. *Light*: *Science & Applications* **15**, 63 (2026).
13. Wang, B. X. et al. Dielectric-based metamaterials for near-perfect light absorption. *Advanced Functional Materials* **34**, 2402068 (2024).
14. Li, Y. & Hong, M. H. Parallel laser micro/nano-processing for functional device fabrication. *Laser & Photonics Reviews* **14**, 1900062 (2020).
15. Zhu, Y. et al. Metasurfaces designed by a bidirectional deep neural network and iterative algorithm for generating quantitative field distributions. *Light*: *Advanced Manufacturing* **4**, 9 (2023).
16. Wang, T. Q. et al. Ultrasensitive bionic photonic-electronic skin with wide red-shift mechanochromic response. *Light*: *Advanced Manufacturing* **6**, 20 (2025).
17. Qi, B. X. et al. A near-perfect metamaterial selective absorber for high-efficiency solar photothermal conversion. *International Journal of Thermal Sciences* **194**, 108580 (2023).
18. Lian, S. S. et al. Biomimetic seaweed photonic graphene for high-performance broadband, self-powered, and polarized image photodetectors. *Chemical Engineering Journal* **522**, 167291 (2025).

19. Leng, B. R. et al. Meta-device: advanced manufacturing. *Light*: *Advanced Manufacturing* **5**, 5 (2024).
20. Cui, K. H. & Wardle, B. L. Breakdown of native oxide enables multifunctional, free-form carbon nanotube–metal hierarchical architectures. *ACS Applied Materials & Interfaces* **11**, 35212-35220 (2019).
21. Saeed, M. et al. Recent advances in carbon nanotubes, graphene and carbon fibers-based microwave absorbers. *Journal of Alloys and Compounds* **970**, 172625 (2024).
22. Kiani, F. et al. Ultra-broadband and omnidirectional perfect absorber based on copper nanowire/carbon nanotube hierarchical structure. *ACS Photonics* **7**, 366-374 (2020).
23. Hizukuri, M. et al. Carbon-nanotube-based all-dielectric near-infrared perfect absorbers. *ACS Photonics* **12**, 6984-6993 (2025).
24. Ye, Y. Q., Jin, Y. & He, S. L. Omnidirectional, polarization-insensitive and broadband thin absorber in the terahertz regime. *Journal of the Optical Society of America B* **27**, 498-504 (2010).
25. Yu, P. Q. et al. Ultra-wideband solar absorber based on refractory titanium metal. *Renewable Energy* **158**, 227-235 (2020).
26. Ma, W., Wen, Y. Z. & Yu, X. M. Broadband metamaterial absorber at mid-infrared using multiplexed cross resonators. *Optics Express* **21**, 30724-30730 (2013).
27. Zhang, Z. et al. Absorption properties and mechanisms of metallic moth-eye structures. *Optics Communications* **540**, 129487 (2023).
28. Liu, X. Y. et al. An ultra-broadband solar absorber based on the biomimetic moth-eye-shaped titanium nitride nanostructures. *Physica B*: *Condensed Matter* **716**, 417757 (2025).
29. Kobayashi, M. et al. Broadband light absorber of gold-coated moth-eye film. *Optical Materials Express* **9**, 3744-3752 (2019).
30. Hakamada, Y. et al. Carbon-coated moth-eye structure: an ultrabroadband THz-DUV near-perfect absorber. *Advanced Optical Materials* **13**, 2500948 (2025).
31. Liu, C. et al. Realization of perfect selective absorber based on multipole modes in all-dielectric moth-eye structure. *Optics Express* **27**, 5703-5718 (2019).
32. Dong, X. X. & Chen, L. S. Ultrabroadband plasmonic absorber based on biomimetic compound eye structures. *IEEE Photonics Journal* **10**, 5700207 (2018).
33. Ren, Z. Y. et al. Bioinspired structured metal-insulator-metal metamaterials with gradient resonator for high efficiency and solar selective absorption. *Small* **21**, 2501698 (2025).
34. Zaman, S. et al. *Coscinodiscus* diatom inspired bi-layered photonic structures with near-perfect absorptance accompanied by tunable absorption characteristics. *Optics Express* **28**, 25007-25021 (2020).
35. Xie, X. H. et al. Diatom cribellum-inspired hierarchical metamaterials: unifying perfect absorption toward subwavelength color printing. *Advanced Materials* **36**, 2403304 (2024).
36. Losic, D. et al. Rapid fabrication of micro- and nanoscale patterns by replica molding from diatom biosilica. *Advanced Functional Materials* **17**, 2439-2446 (2007).
37. Ren, Z. Y. et al. Ultra-broadband perfect absorbers based on biomimetic metamaterials with dual coupling gradient resonators. *Advanced Materials* **37**, 2416314 (2025).
38. Liao, Q. H. et al. Bio-inspired ultrathin perfect absorber for high-performance

photothermal conversion. *Advanced Materials* **36**, 2313366 (2024).

39. Jouttijärvi, S. et al. Benefits of bifacial solar cells combined with low voltage power grids at high latitudes. *Renewable and Sustainable Energy Reviews* **161**, 112354 (2022).
40. Guerrero-Lemus, R. et al. Bifacial solar photovoltaics – a technology review. *Renewable and Sustainable Energy Reviews* **60**, 1533-1549 (2016).
41. Shin, M. J. et al. Semitransparent and bifacial ultrathin Cu(In,Ga)$Se_2$ solar cells via a single-stage process and light-management strategy. *Nano Energy* **82**, 105729 (2021).
42. Song, Y. T. et al. Graphene-based double-sided light absorption evaporators with enhanced water supply for solar desalination. *ACS Applied Nano Materials* **7**, 996-1008 (2024).
43. Yang, S. C. et al. Efficiency boost of bifacial Cu(In,Ga)$Se_2$ thin-film solar cells for flexible and tandem applications with silver-assisted low-temperature process. *Nature Energy* **8**, 40-51 (2023).
44. Huang, T. Y. et al. Experimental realization of ultrathin, double-sided metamaterial perfect absorber at terahertz gap through stochastic design process. *Scientific Reports* **5**, 18605 (2015).
45. Gao, P. Q. et al. Large-area nanosphere self-assembly by a micro-propulsive injection method for high throughput periodic surface nanotexturing. *Nano Letters* **15**, 4591-4598 (2015).
46. Gao, X. et al. The dry-style antifogging properties of mosquito compound eyes and artificial analogues prepared by soft lithography. *Advanced Materials* **19**, 2213-2217 (2007).
47. Thornton, J. A. Influence of apparatus geometry and deposition conditions on the structure and topography of thick sputtered coatings. *Journal of Vacuum Science and Technology* **11**, 666-670 (1974).
48. Augustine, J. A. & Hodges, G. B. Variability of surface radiation budget components over the U.S. from 1996 to 2019—has brightening ceased?. *Journal of Geophysical Research*: *Atmospheres* **126**, e2020JD033590 (2021).